Numerical approach for the determination of multi-mechanisms of the densification of TiAl by spark plasma sintering

Antoine van Der Laan, R. Epherre, Claude Estournès

Numerical approach for the determination of multi-mechanisms of the densification of TiAl by spark plasma sintering

A. Van der Laan[a,b], R. Epherre[b], C. Estournès[a,*]

[a] CIRIMAT, Université de Toulouse, CNRS, Université Toulouse 3 – Paul-Sabatier, 118 Route de Narbonne, 31062 Toulouse cedex 9 – France

[b] Norimat, 51 Rue de l'Innovation, 31670 Labège

* Corresponding author: estournes@chimie.ups-tlse.fr

Abstract

One of the main benefits of numerical modeling is that it can be used to have access to some features, which are not accessible experimentally. For example, it is quite complicated to determine experimentally the sintering mechanisms that occur during spark plasma sintering (SPS). The obtention of a mechanical model of the SPS is usually done with only one mechanism. However, it has been shown that sometimes more than one mechanism is involved in the densification process as it is the case for TiAl. Thus, an innovative multi-mechanisms approach was developed, which considers the simultaneous effect of two mechanisms on the densification of TiAl. First the two sintering mechanisms of the material were identified numerically. Then, with the method developed in this work, the influence of each mechanism can be decorrelated and interpreted to determine their role during spark

plasma sintering. The approach developed here can be applied to any material and shows how numerical modelling can be used to better understand the sintering mechanisms of the SPS.

Keywords

Spark plasma sintering, Numerical modelling, Creep parameters, multi-mechanisms

1. Introduction

Spark plasma sintering (SPS) is an electric current assisted sintering (ECAS) technique that is used to consolidate a wide range of materials with lower processing time and costs compared to conventional techniques like hot pressing (HP) or hot isostatic pressing (HIP) [1]. The application of a uniaxial pressure combined with Joule heating allows to sinter materials with high heating rates, and at a temperature lower than their melting points or decomposition temperature [2]. SPS is a versatile process, since it has been used to sinter materials like ceramics, metals, alloys, or composites [3,4]. Besides its low processing time, the SPS process also tends to improve the mechanical properties of the materials [5–7]. This is obtained thanks to a controlled microstructure throughout the process. All these benefits make the SPS a competitive process because it offers the opportunity to produce high added value materials with reduced production costs [8].

A large number of publications focus on the study of the influence of processing parameters on the densified material properties and its densification mechanisms [5,9,10]. This shows the increasing interest of the scientific community for the understanding and control of the mechanisms occurring during spark plasma sintering. Numerical simulation appears to be an appropriate solution to tackle these new challenges, since it can be used to better understand, predict, or optimize the process. Understanding the process allows to establish a relationship

between the operating conditions and the electric, thermal, mechanical, and/or microstructural features of the sintered material during sintering. Once this is achieved, the numerical model can be used as a predictive tool to identify for example thermal gradients [11,12], stress concentrations [13] or microstructure inhomogeneities [14]. This allows to anticipate the effects of several parameters on the densification of the material, and thus, to significantly reduce the number of experiments to reach the desired product. Finally, numerical simulation can be used to optimize the sintering parameters or apparatus in order to reduce the production time and costs, while enhancing material properties and the SPS capabilities. For example, this has been used in the literature to produce multi-samples by SPS [15].

However, to use the numerical simulation to its full potential, it has first to be thoroughly calibrated. The developed model has to accurately correspond to the mechanisms involved, but such a precise simulation could be difficult to implement. Obtaining a fully coupled simulation of the SPS process requires first an accurate electro-thermal model. SPS uses indeed Joule effect to heat up the apparatus, and most of the sintering mechanisms are temperature dependent [16–18]. A numerical approach to develop an accurate electro-thermal model of the spark plasma sintering of any material has been developed in a previous study [19]. Then, creep and sintering considerations needs to be added to the model to predict the densification of the material. To implement these aspects into the model, the most commonly used method in the literature is based on a Norton-Green model [20] involving creep parameters combined with porosity functions [21–23]. The values of the creep parameters correspond to a specific sintering mechanism and they can be determined empirically [24,25]. A numerical method has also been developed in a previous study [26], which allows to obtain these parameters through only one experiment. However, to the best of our knowledge, only one mechanism is considered responsible for the densification. Realistically, it is likely that more than one mechanism is involved in the sintering as it has been showed experimentally

for several materials [27–29]. To perfect the model an innovative numerical multi-mechanisms approach of the sintering is developed in this work. This method will be applied to a titanium aluminide (TiAl), but it is developed to be used on any other material.

2. Experimental and computational methodology

2.1. Materials and methods

The material used in this work is a titanium aluminide (TiAl) powder TiAl-4822, composed of 48%-at aluminum, 2%-at niobium et 2%-at chromium. The powder is produced by Praxair and has a grain size between 45 and 105µm (with an average of 75.4µm).

All the spark plasma sintering experiments were performed at the Plateforme Nationale CNRS de Frittage Flash located at the Université Toulouse 3, Paul Sabatier (Toulouse, France) with a Dr.Sinter 2080 unit, SPS Syntex Inc., (Japan). The TiAl powder was placed in a graphite mold with an inner diameter of 36mm and an outer diameter of 70mm. A graphite foil (PERMA-FOIL®Toyo Tanso) was placed on the inside wall of the die and at the interface between the punches and the powder. To minimize the heat loss at the surface of the die, a graphite felt was placed on its outside wall. The SPS column, composed of the electrodes, spacers, punches, mold, and sample, is presented in Figure 1.

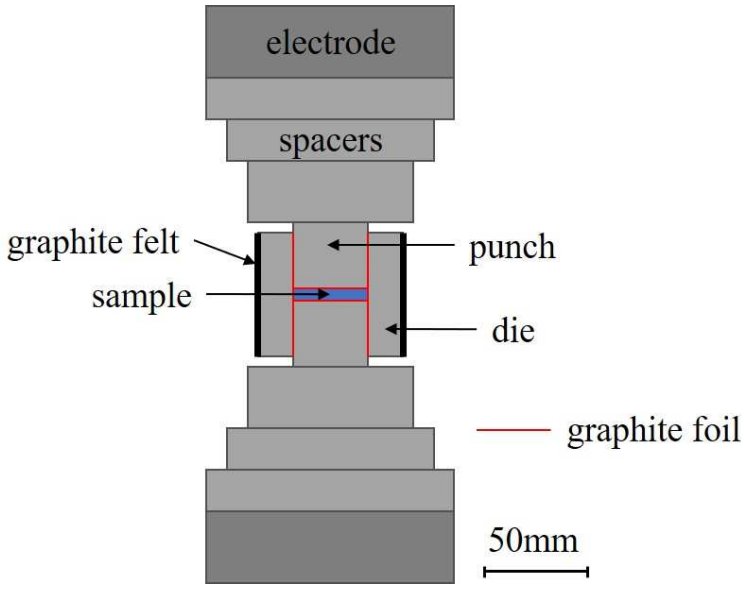

Figure 1 : SPS configuration used to sinter the 36mm TiAl sample

The electric current sent in the system is regulated through a PID regulation that controls the difference between a set control temperature and the one measured in a 3mm hole (with a diameter of 1.8mm) located in the outside wall of the die. This temperature is measured using a lateral pyrometer (IR-AH series Chino).

To sinter the TiAl powder, the setpoint temperature is first set at 600°C for five minutes, because the lower limit of the temperature range measured by the pyrometer is 570°C. Then the temperature is increased at a rate of 100°C/min up to full densification of the powder, which is reached at 1150°C. Once this temperature is reached, the power is switched off and the pressure released.

During the SPS trial, the machine records the electric current and voltage, the control temperature, and the displacement of the electrodes. This displacement is induced by the densification of the powder and the dilation of the whole apparatus. Thus, to extract only the displacement due to the sintering of the material, another SPS cycle is launched on the densified sample [26]. When the system has cooled down, the same SPS cycle is applied to

measure the displacement of the column without the influence of the densification. By subtracting the two displacement curves from the two experiments, it is possible to calculate the evolution of the relative density during the sintering as illustrated Figure 2. After the SPS experiments, the density of the sample was measured at 100% using the Archimedes technique.

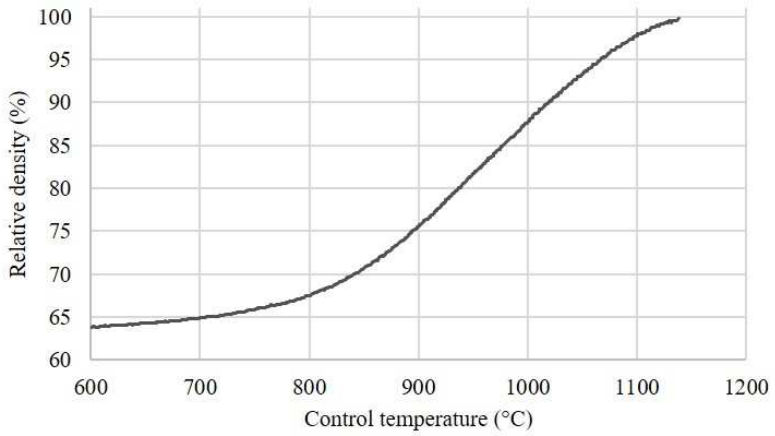

Figure 2: Evolution of the relative density of a 36mm TiAl sample

All the numerical calculation was realized with Comsol Multiphysics©. The SPS apparatus was modeled in 2D-axisymetric and treated as a union. All the limit conditions were detailed in previous works [19,26]. The electrical, thermal, and mechanical properties used in the model are presented in Table 1. The porosity dependence of the properties of the TiAl were implemented using the work of Orrù *et al*. [3].

Table 1: Physical properties of Inconel, graphite and TiAl [11,30]

	Inconel	Graphite	TiAl
Heat capacity ($J.kg^{-1}.K^{-1}$)	$344 + 2.50 \times 10^{-1} T$	$34.27 + 2.72 T - 9.60 \times 10^{-4} T^2$	$583 + 9.40 \times 10^{-2} T$

Thermal conductivity ($W.m\text{-}1.K^{-1}$)	$10.1 + 1.57 \times 10^{-2} T$	$123 - 6.99\ 10^{-2} T + 1.55 \times 10^{-5} T^2$	$9.47 + 1.19 \times 10^{-2} T$
Electrical resistivity ($\Omega.m$)	$9.82 \times 10^{-7} + 1.60 \times 10^{-10} T$	$1.70 \times 10^{-5} - 1.87 \times 10^{-8} T + 1.26 \times 10^{-11} T^2 - 2.44 \times 10^{-15} T^3$	$4.06 \times 10^{-7} + 6.45 \times 10^{-10} T$
Young's modulus (GPa)	204	13	120
Poisson's coefficient	0.32	0.2	0.34
Density ($kg.m^{-3}$)	8430	1904-0.01414 T	3960

2.2. Electro-thermal and mechanical simulation

The development of an accurate simulation of the sintering of the TiAl powder was described in a previous study [19]. This study shows a method that allows to numerically determine the electrical and thermal contact resistances at the internal surface of the graphite mold. With this method it is possible to obtain an accurate description of both the electrical and thermal behavior of the entire SPS column (electrodes, spacers, punches, mold and sample). This is illustrated Figure 3 with the comparison between the experimental and simulated evolution of the current and the temperature at several position of a TiAl sample with a diameter of 36mm.

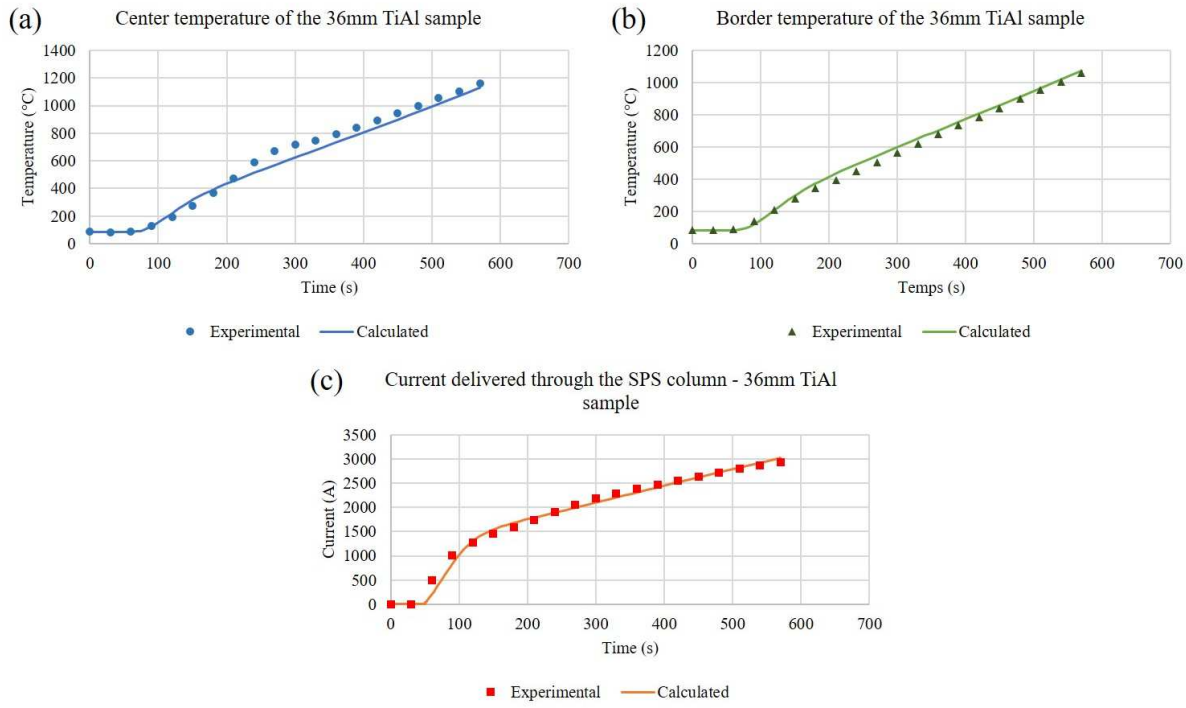

Figure 3: Evolution of the temperature at the center (a) and 3mm away from the border of the TiAl sample (b). Evolution of the current through the SPS column (c)

In this work, the goal is to add to this model the creep and sintering mechanism considerations to obtain a fully coupled electro-thermal and mechanical (ETM) model. Due to the uniaxial pressure applied during the sintering, compressive creep mechanisms must be considered. These are described in the sample using a Norton-Green creep power law equation [31]:

$$\dot{\varepsilon}_{eq} = A{\sigma_{eq}}^{n} \quad (1)$$

Where $\dot{\varepsilon}_{eq}$ et σ_{eq} are the equivalent strain rate and the equivalent stress, the parameter n is the power law creep exponent and A is a temperature dependent parameter defined as such:

$$A = A_0 exp\left(-\frac{Q}{RT}\right) \quad (2)$$

Where A_0 is a pre-exponential factor, Q the creep activation energy, R the universal gas constant and t the temperature. The simulation of the creep mechanism of the TiAl sample requires the identification of the creep parameters n, Q and A_0.

With the Norton-Green creep power law, the sample is considered as a dense visco-plastic material [31]. However, during the SPS trial, the TiAl starts as a powder with an initial relative density of 65%, and then reaches full density. Thus, to take into account the densification of the sample, porosity functions are added in the model with the approach of Abouaf [21]. This approach consists in the introduction of a dissipative potential in the expression of the strain rate tensor. This dissipative potential can be expressed using to porosity functions as follow:

$$\underline{\dot{\varepsilon}} = \frac{\dot{\varepsilon}_{eq}}{\sigma_{eq}}\left(\frac{3}{2}c\underline{\sigma} + \left(f - \frac{1}{2}c\right)I_1\mathbb{I}\right) \quad (3)$$

Where I_1 is the invariant of the stress tensor, and c and f are the porosity functions defined as such:

$$\begin{cases} c = 1 + \alpha f \\ f = K_f\left(\frac{1-\rho}{\rho - \rho_{cr}}\right)^{\beta} \end{cases} \quad (4)$$

Where α, β and K_f are parameters that needs to be determined for each material. However, in a previous work, D. Martins *et al*. [32] have determined experimentally those parameters. Those parameters were identified on a TiAl powder using two sets of quite complex experiments: a uniaxial free compaction and a confined compression on porous samples. In this work, the same powder, the same SPS apparatus and similar sintering conditions were used. Thus, the decision was made to use the porosity function determined by D. Martins *et al*. [32]:

$$\begin{cases} c = 1 + 2.9f \\ f = 4.97\left(\frac{1-\rho}{\rho - 0.52}\right)^{1.51} \end{cases} \quad (5)$$

In the equation (3), the ratio $\frac{\sigma_{eq}}{\dot{\varepsilon}_{eq}}$ can be expressed using the Norton-Green creep law equation (1) and the following relation developed by Abouaf et al. [21] between the equivalent stress and the porosity function and the invariants of the stress tensors I_1 and J_2:

$$\sigma_{eq} = \sqrt{3cJ_2 + fI_1{}^2} \tag{6}$$

To consider the modification of the density in the numerical model, the expression of conservation of mass is implemented as follow [21]:

$$\frac{\dot{\rho}}{\rho} = -tr(\underline{\dot{\epsilon}}) = -\frac{3\dot{\varepsilon}_{eq} f I_1}{\sigma_{eq}} \tag{7}$$

To be able to use the model and describe the evolution of the density of the TiAl during spark plasma sintering, the creep parameters n, Q and A_0 of the equations (1) and (2) need to be determined.

2.3. Numerical identification of the creep parameters

In the literature, the identification of the creep parameters is usually done using an experimental method [25,32]. In a previous work, a numerical method has been developed that allows to obtain similar results but with only one SPS trial [26]. With this approach the creep parameters are optimized numerically using a curve fitting algorithm. The experimental evolution of the relative density is fed into the curve fitting algorithm to find the set of parameters (n, Q and A_0) that will best fit the experimental data. This technique gave good results on two different materials (alumina and TiAl) and for different sample sizes.

In their work, D. Martins *et al*. [32] not only identified the porosity functions c and f, but they also determined experimentally the creep parameters n, Q and A_0. Those parameters were

determined using SPS trials, which is more accurate to describe the behavior of the powder spark plasma sintering. However, with this set of parameters, the model was only able to fit the sintering occurring at high temperatures, i.e. for a relative density higher than 80%. The conclusion of this study was that not only one mechanism is responsible of the sintering of the TiAl but at least two: one at low temperatures and another at high temperatures. It is stated that the low temperature mechanism creates bonds between the grains (without affecting the relative density), which leads to a porous 3D-object. For high temperature, the second mechanism, which nature was not specified by the author, is responsible of the material densification. This multi-mechanism hypothesis was also confirmed numerically in our previous work [26]. The curve fitting algorithm was not able to find a set of creep parameters that fit the whole densification curve. Since the algorithm explores a wide range of combination of parameters, this indicates that probably not only one but at least two mechanisms occur during the sintering of TiAl.

For the remaining of the study, it is assumed that two mechanisms are responsible for the sintering of TiAl: one at low temperatures and one at high temperatures. To decorrelate the influence of the two mechanisms on the densification curve, the experimental data was arbitrarily divided in two parts: one at low temperatures (for a relative density below 80%) and one at high temperatures (for a relative density higher than 80%). Then the two parts were fed into the curve fitting algorithm, which was able to identify two distinct mechanisms as illustrated Figure 4. A sensitivity study has been performed on the chosen threshold value of 80% with an offset of +/-5%. This has not affected significantly the results.

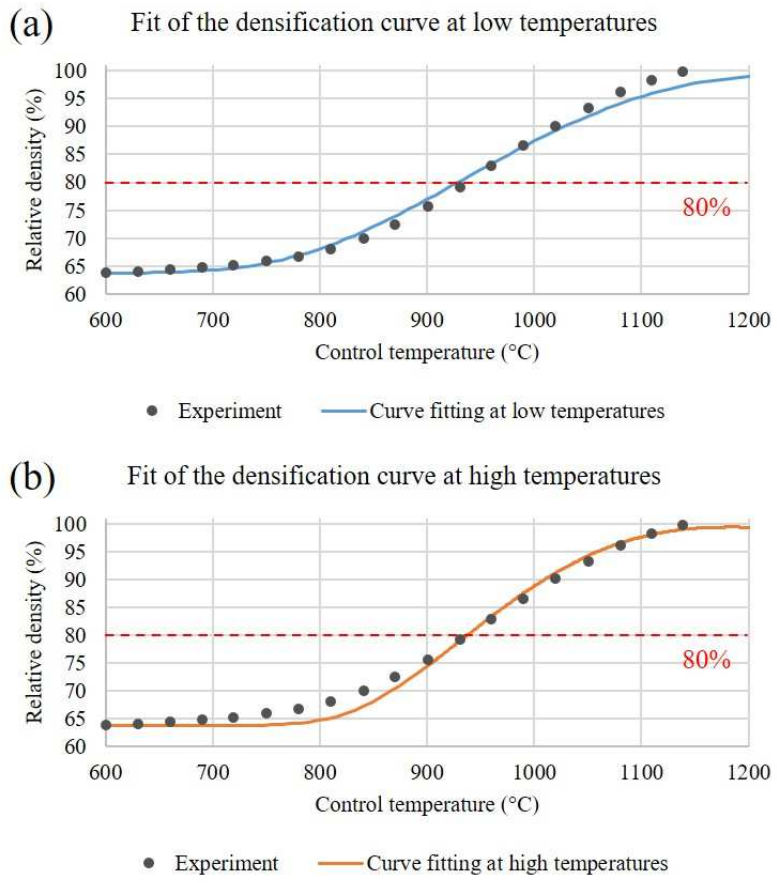

Figure 4: Results of the curve fitting of the densification for low (a) and high temperatures (b)

In the range of temperature considered for each mechanism, the gap between the experimental and numerical data is less than 1%. The values of the creep parameters are reported in Table 2.

Table 2: Calculated creep parameters compared to the ones determined experimentally by D. Martins et al. [32]

	n	**Q (kJ/mol)**	**A_0 ($s^{-1}.Pa^{-n}$)**
Calculated (relative density <80%)	1.57	220	3.76×10^{-9}
Calculated (relative density >80%)	2.57	446	3.17×10^{-9}
D. Martins *et al.* [32]	2.81	414	4.33×10^{-9}

The parameters identified numerically for the high temperatures are in a very good agreement with the ones identified experimentally by D. Martins *et al*. [32] with in situ SPS trials. In their work, U. Hofmann et al. [33] also identified at high temperature under air, the creep parameters of dense TiAl ingots exhibiting full lamellar microstructure, but the values were obtained with a compressive test for pressures from 50 to 390MPa. Although their conditions slightly differ from the SPS ones used in this work (starting from a powder with bi-phased microstructure to full lamellar dense specimen at the end of the sintering cycle), they determined a value of n=3 and Q=350kJ/mol which are quite comparable to the ones found numerically. This confirms the effectiveness of the numerical method as well as the probability the more than one mechanism occurs during the spark plasma sintering of TiAl since it was showed by two different methods.

According to the literature [24,34], a stress exponent value close to 1, 2 and 3 are associated respectively with a diffusion, grain boundary sliding (GBS) and plastic deformation mechanisms. The values of n identified in Table 2 suggest that at low temperature, the diffusion and GBS mechanisms are involved in the densification of TiAl, whereas at high temperature it is a combination of GBS and plastic deformation.

Now that the set of creep parameters of the two mechanisms were determined, the objective is to find a way to combine them to obtain a single curve of the relative density.

3. Results and discussion

3.1. Sequential approach

Considering the two curves in Figure 4, a first naive approach would be to combine the two mechanisms sequentially. The first mechanism was obtain using the experimental data of the relative density below 80%, and the second one for values higher than 80%. Thus, the first

creep parameters can be used up to 80% of relative density and the second set for higher values. The obtained curve is presented Figure 5.

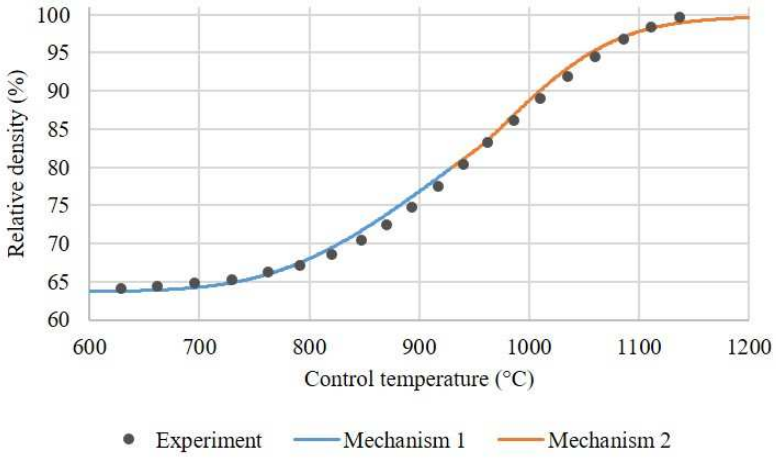

Figure 5: Relative density of a TiAl sample obtained with the sequential approach

The overall gap between the experimental and numerical data is below 1%, which constitutes a very good results for the simulation of the sintering. However, by looking at the evolution of the ratio $\frac{\dot{\rho}}{\rho}$ from the equation (7) in Figure 6, it appears that there is a discontinuity in the curve when the model switches from one mechanism to another.

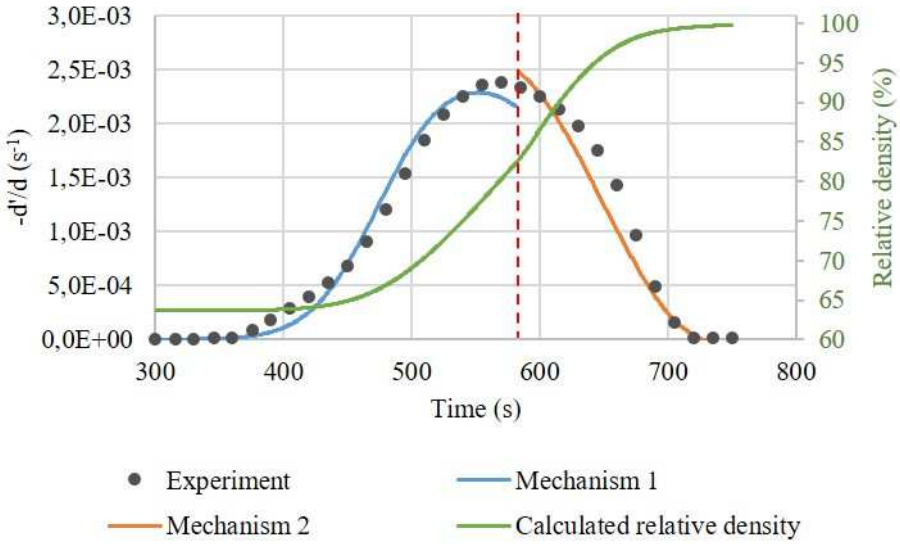

Figure 6: Evolution of the conservation of mass obtained with the sequential approach

Since the equation (7) corresponds to the conservation of mass, its evolution has to be continuous. Thus, the sequential approach gives a good approximation of the relative density, but it does not relate what really happens mechanistically. The fact that the two mechanisms were considered to happen sequentially cannot be validated. It seems that considering a range of temperatures were both mechanisms occur simultaneously constitutes a more realistic assumption.

3.2. Simultaneous approach

The two distinct mechanisms identified, with their respective set of creep parameters reported in Table 2, will be now considered to occur simultaneously over a range of temperature. To do so, two weight functions α_1 and α_2, corresponding to the weight of each mechanism during the sintering, need to be introduced. These functions must be comprised between 0 and 1. Several types of functions were tested (linear functions for example), but it is a sigmoidal form, described in equation (8), that showed the most accurate results:

$$\begin{cases} \alpha_1(T) = 1 - \dfrac{1}{1 + \exp(-a_m(T - T_m))} \\ \alpha_2(T) = 1 - \alpha_1(T) \end{cases} \tag{8}$$

Where a_m and T_m are two parameters that need to be determined. This type of function was chosen due to its use in several scientific fields to describe phase transitions for example [35]. These two weight functions were implemented in the model by modifying the conservation of mass equation as such:

$$tr(\underline{\dot{\varepsilon}}) = -\alpha_1(T)\left(\frac{\dot{\rho}}{\rho}\right)_{mechanism\ 1} - \alpha_2(T)\left(\frac{\dot{\rho}}{\rho}\right)_{mechanism\ 2} \tag{9}$$

Where the ratio $\frac{\dot{\rho}}{\rho}$ of each mechanism is expressed using the creep parameters reported in Table 2. To identify the two parameters a_m and T_m from equation (8), the same curve fitting algorithm used to find the creep parameters was used. Thus, the parameters a_m and T_m are optimized numerically to find the best fit with the evolution of the relative density. The values obtained for a_m is $0.038K^{-1}$ and T_m is 1214°C. The comparison between the experimental and the numerical relative density is presented in Figure 7.

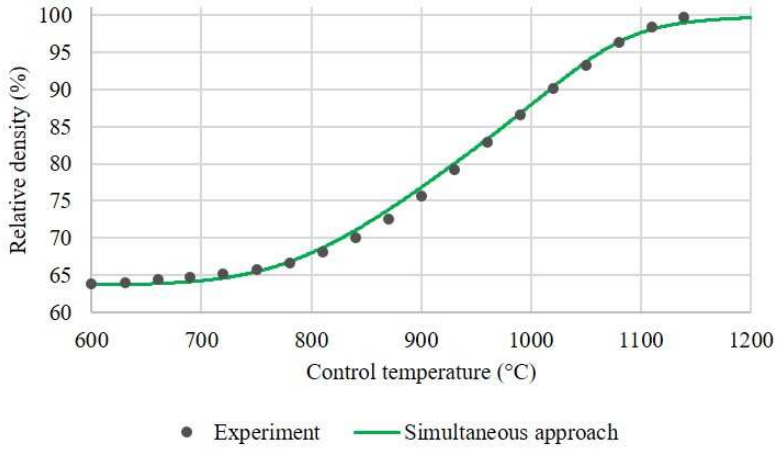

Figure 7: Relative density of a TiAl sample obtained with a simultaneous approach

The obtained curve is in a very good agreement with the experimental data with a maximal gap between the two of less than 1%. Moreover, looking at the conservation of mass curve in Figure 8, there are no discontinuity unlike the sequential method. This shows that this method can accurately predicts the evolution of the relative density of a multi-mechanism sintering, which was, to the best of our knowledge, never been done before.

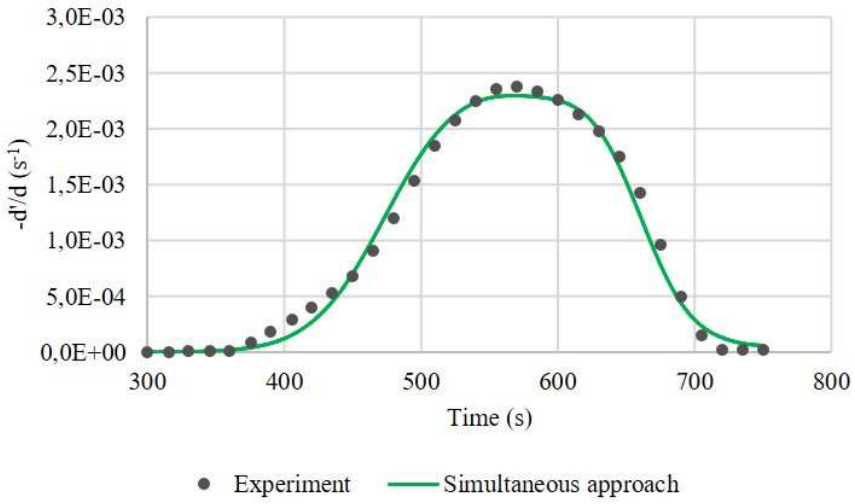

Figure 8: Evolution of the conservation of mass obtained with the simultaneous approach

Another benefit of this method is that the influence of each mechanism can be extracted from the experimental curve as presented Figure 9, where the two weight functions are plotted. It shows that the first mechanism is alone responsible for the sintering of the TiAl up to a relative density of 73% (which corresponds to a temperature of 880°C). Then, the two mechanisms occur simultaneously up to a density of 96% (or a temperature of 1075°C). Lastly, the second mechanism is the only one remaining for the end of the densification. Also, the parameter T_m identified from equation (8) has a physical meaning since it corresponds to a transition temperature. The value found for this parameter is 1214°C, which is in the range of the transition between the duplex and lamellar phase [29]. This phase change could explain the change in the creep mechanism seen between low and high temperatures.

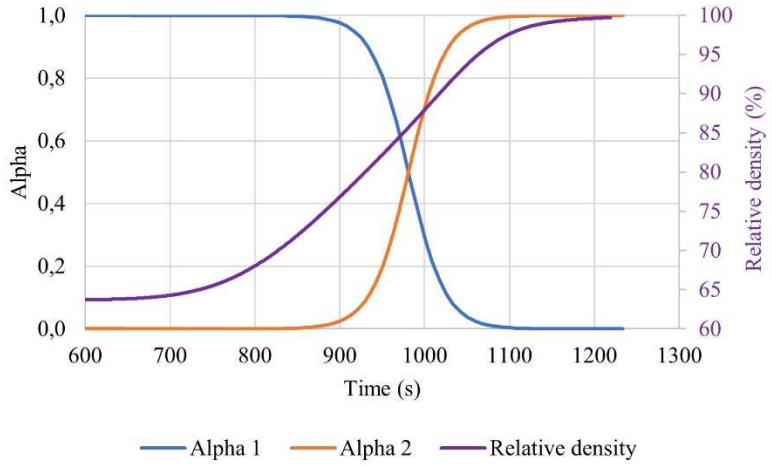

Figure 9: Evolution of the weight function of each mechanism during the sintering of a TiAl sample

4. Conclusions and future work

This study was dedicated to the development of an innovative simultaneous multi-mechanism consideration of the sintering. In most works, the sintering of the studied material is considered as induced by only one mechanism. However, it has been proven experimentally that in some case, more than one mechanism can occur during the sintering, as it is the case for the spark plasma sintering of TiAl.

Thanks to a numerical method, two different mechanisms were identified as responsible for the sintering of TiAl at low and high temperatures respectively. The mechanism identified for the high temperatures is in an agreement with the one determined with an experimental in situ SPS method. This shows the effectiveness of this numerical approach to easily extrapolate the creep parameters from the experimental densification curve, and without any complex tooling or experimental campaigns. However, the mechanism identified for low temperatures still needs to be validate experimentally.

With two (or more) mechanisms responsible for the sintering of a material, the goal is to find a way to combine the influence of the two mechanisms to obtain a single simulated

densification curve. If a sequential method (i.e. considering the mechanisms one after the other) gave a good approximation of the relative density, it failed to describe how those mechanisms really governs the sintering. Thus, an innovative simultaneous multi-mechanism method was developed. This method is based on the introduction of weight functions, which describe the influence of each identified mechanisms during the densification. With this method, the model was able to give an accurate prediction of the evolution of the relative density, as well as extrapolate from the experimental curve the influence of each mechanisms at each temperature.

The main benefit of the multi-mechanisms approach developed here, is that it can be used on any material provided that several mechanisms are responsible of the sintering. Indeed, this approach was developed here on TiAl, but it is totally independent of the material considered. Moreover, the approach of Abouaf was chosen to describe the sintering of the TiAl but another approach (like the one of Olevsky *et al*. for example) could be used without affecting the effectiveness of the method.

The main difficulty of the multi-mechanisms approach relies on the identification of the different mechanisms. If the identification of the sintering mechanisms could have been done experimentally, here this was done numerically, since of the goal of this work is to implement a method that can be efficiently and easily used with a wide range of materials or configurations.

In this study, it was assumed that only two mechanisms occurred: one at low temperatures and another at high temperatures. The end results seem to accurately correspond to the experimental data, which tends to validate the two mechanisms hypothesis. However, the multi-mechanism approach could have been used on three mechanisms, but the more mechanisms are considered, the harder it is to extrapolate the weight of each of them.

Acknowledgements

We thank Norimat for the technical and financial support. The SPS experiments were performed at the Plateforme Nationale CNRS de Frittage-Flash (PNF2/CNRS Toulouse).

This work was supported by the Association Nationale Recherche Technologie (ANRT) as part of the CIFRE (Industrial Agreement of Formation by Research) contract n°2017/1026; and the Programme Opérationnel FEDER-FSE Midi-Pyrénées et Garonne 2014-2020 as part of the CERAPRINT project n°17014462.

References

[1] S. Grasso, Y. Sakka, G. Maizza, Electric current activated/assisted sintering (ECAS): A review of patents 1906-2008, Sci. Technol. Adv. Mater. 10 (2009). https://doi.org/10.1088/1468-6996/10/5/053001.

[2] O. Guillon, J. Gonzalez-Julian, B. Dargatz, T. Kessel, G. Schierning, J. Räthel, M. Herrmann, Field-assisted sintering technology/spark plasma sintering: Mechanisms, materials, and technology developments, Adv. Eng. Mater. 16 (2014) 830–849. https://doi.org/10.1002/adem.201300409.

[3] R. Orrù, R. Licheri, A.M. Locci, A. Cincotti, G. Cao, Consolidation/synthesis of materials by electric current activated/assisted sintering, Mater. Sci. Eng. R Reports. 63 (2009) 127–287. https://doi.org/10.1016/j.mser.2008.09.003.

[4] Z.Y. Hu, Z.H. Zhang, X.W. Cheng, F.C. Wang, Y.F. Zhang, S.L. Li, A review of multi-physical fields induced phenomena and effects in spark plasma sintering: Fundamentals and applications, Mater. Des. 191 (2020) 108662. https://doi.org/10.1016/j.matdes.2020.108662.

[5] R. Chaim, M. Levin, A. Shlayer, C. Estournes, Sintering and densification of nanocrystalline ceramic oxide powders: A review, Adv. Appl. Ceram. 107 (2008) 159–169. https://doi.org/10.1179/174367508X297812.

[6] R. Chaim, R. Marder, C. Estournés, Z. Shen, Densification and preservation of ceramic nanocrystalline character by spark plasma sintering, Adv. Appl. Ceram. 111 (2012) 280–285. https://doi.org/10.1179/1743676111Y.0000000074.

[7] E.A. Olevsky, W.L. Bradbury, C.D. Haines, D.G. Martin, D. Kapoor, Fundamental aspects of spark plasma sintering: I. Experimental analysis of scalability, J. Am.

Ceram. Soc. 95 (2012) 2406–2413. https://doi.org/10.1111/j.1551-2916.2012.05203.x.

[8] J.P. Kelly, O.A. Graeve, Spark Plasma Sintering as an Approach to Manufacture Bulk Materials: Feasibility and Cost Savings, Jom. 67 (2015) 29–33. https://doi.org/10.1007/s11837-014-1202-x.

[9] J.M. Calderón-Moreno, A.R. de Arellano-López, A. Domínguez-Rodríguez, J.L. Routbort, Microstructure and creep properties of alumina/zirconia ceramics, J. Eur. Ceram. Soc. 15 (1995) 983–988. https://doi.org/10.1016/0955-2219(95)00070-B.

[10] E. Olevsky, L. Froyen, Constitutive modeling of spark-plasma sintering of conductive materials, Scr. Mater. 55 (2006) 1175–1178. https://doi.org/10.1016/j.scriptamat.2006.07.009.

[11] G. Molénat, L. Durand, J. Galy, A. Couret, Temperature Control in Spark Plasma Sintering: An FEM Approach, J. Metall. 2010 (2010) 1–9. https://doi.org/10.1155/2010/145431.

[12] Y. Achenani, M. Saâdaoui, A. Cheddadi, G. Bonnefont, G. Fantozzi, Finite element modeling of spark plasma sintering: Application to the reduction of temperature inhomogeneities, case of alumina, Mater. Des. 116 (2017) 504–514. https://doi.org/10.1016/j.matdes.2016.12.054.

[13] G. Antou, G. Mathieu, G. Trolliard, A. Maître, Spark plasma sintering of zirconium carbide and oxycarbide: Finite element modeling of current density, temperature, and stress distributions, J. Mater. Res. 24 (2009) 404–412. https://doi.org/10.1557/jmr.2009.0039.

[14] C. Manière, L. Durand, A. Weibel, C. Estournès, Spark-plasma-sintering and finite element method: From the identification of the sintering parameters of a submicronic

α-alumina powder to the development of complex shapes, Acta Mater. 102 (2016) 169–175. https://doi.org/10.1016/j.actamat.2015.09.003.

[15] C. Manière, U. Kus, G. Chevallier, A. Weibel, L. Durand, J. Huez, D. Delagnes, C. Estournès, How to overcome the main challenges of SPS technology: Reproducibility, multi-samples and elaboration of complex shapes, in: G. Cao, C. Estournès, J. Garay, R. Orrù (Eds.), Spark Plasma Sinter. 1st Ed. Curr. Status, New Dev. Challenges, Elsevier, 2019: pp. 77–108. https://doi.org/10.1016/b978-0-12-817744-0.00003-9.

[16] W. Chen, U. Anselmi-Tamburini, J.E. Garay, J.R. Groza, Z.A. Munir, Fundamental investigations on the spark plasma sintering/synthesis process: I. Effect of dc pulsing on reactivity, Mater. Sci. Eng. A. 394 (2005) 132–138. https://doi.org/10.1016/j.msea.2004.11.020.

[17] U. Anselmi-Tamburini, S. Gennari, J.E. Garay, Z.A. Munir, Fundamental investigations on the spark plasma sintering/synthesis process: II. Modeling of current and temperature distributions, Mater. Sci. Eng. A. 394 (2005) 139–148. https://doi.org/10.1016/j.msea.2004.11.019.

[18] U. Anselmi-Tamburini, J.E. Garay, Z.A. Munir, Fundamental investigations on the spark plasma sintering/synthesis process: III. Current effect on reactivity, Mater. Sci. Eng. A. 407 (2005) 24–30. https://doi.org/10.1016/j.msea.2005.06.066.

[19] A. Van der Laan, V. Boyer, R. Epherre, C. Estourn, Simple method for the identification of electrical and thermal contact resistances in spark plasma sintering, 41 (2020) 599–610. https://doi.org/10.1016/j.jeurceramsoc.2020.08.073.

[20] R.J. Green, A plasticity theory for porous solids, Int. J. Mech. Sci. 14 (1972) 215–224. https://doi.org/10.1016/0020-7403(72)90063-X.

[21] M. Abouaf, J.L. Chenot, G. Raisson, P. Bauduin, Finite element simulation of hot isostatic pressing of metal powders, Int. J. Numer. Methods Eng. 25 (1988) 191–212. https://doi.org/10.1002/nme.1620250116.

[22] E.A. Olevsky, Theory of sintering: From discrete to continuum, Mater. Sci. Eng. R Reports. 23 (1998) 41–100. https://doi.org/10.1016/S0927-796X(98)00009-6.

[23] E.A. Olevsky, C. Garcia-Cardona, W.L. Bradbury, C.D. Haines, D.G. Martin, D. Kapoor, Fundamental aspects of spark plasma sintering: II. Finite element analysis of scalability, J. Am. Ceram. Soc. 95 (2012) 2414–2422. https://doi.org/10.1111/j.1551-2916.2012.05096.x.

[24] B. Ratzker, M. Sokol, S. Kalabukhov, N. Frage, Creep of polycrystalline magnesium aluminate spinel studied by an SPS apparatus, Materials (Basel). 9 (2016) 1–9. https://doi.org/10.3390/ma9060493.

[25] B. Ratzker, M. Sokol, S. Kalabukhov, N. Frage, Using a spark plasma sintering apparatus as a tool in a compressive creep study of fine-grained alumina, Ceram. Int. 43 (2017) 9369–9376. https://doi.org/10.1016/j.ceramint.2017.04.106.

[26] A. Van der Laan, R. Epherre, G. Chevallier, Y. Beynet, A. Weibel, C. Estournès, Fully coupled electrothermal and mechanical simulation of the production of complex shapes by spark plasma sintering, J. Eur. Ceram. Soc. 41 (2021) 4252–4263. https://doi.org/10.1016/j.jeurceramsoc.2021.02.010.

[27] A.M. Locci, R. Orrù, G. Cao, Modeling of Electric Current Assisted Sintering: An extended fluid-like approach for the description of powders rheological behavior, Chem. Eng. Res. Des. 154 (2020) 283–302. https://doi.org/10.1016/j.cherd.2019.12.001.

[28] C. Manière, G. Lee, J. McKittrick, S. Chan, E.A. Olevsky, Modeling zirconia sintering trajectory for obtaining translucent submicronic ceramics for dental implant applications, Acta Mater. 188 (2020) 101–107. https://doi.org/10.1016/j.actamat.2020.01.061.

[29] D. Martins, F. Grumbach, A. Simoulin, P. Sallot, K. Mocellin, M. Bellet, C. Estournès, Spark plasma sintering of a commercial TiAl 48-2-2 powder: Densification and creep analysis, Mater. Sci. Eng. A. 711 (2018) 313–316. https://doi.org/10.1016/j.msea.2017.11.041.

[30] C. Manière, A. Pavia, L. Durand, G. Chevallier, K. Afanga, C. Estournès, Finite-element modeling of the electro-thermal contacts in the spark plasma sintering process, J. Eur. Ceram. Soc. 36 (2016) 741–748. https://doi.org/10.1016/j.jeurceramsoc.2015.10.033.

[31] C. Manière, U. Kus, L. Durand, R. Mainguy, J. Huez, D. Delagnes, C. Estournès, Identification of the Norton-Green Compaction Model for the Prediction of the Ti–6Al–4V Densification During the Spark Plasma Sintering Process, Adv. Eng. Mater. 18 (2016) 1720–1727. https://doi.org/10.1002/adem.201600348.

[32] D. Martins, F. Grumbach, C. Manière, P. Sallot, K. Mocellin, M. Bellet, C. Estournès, In-situ creep law determination for modeling Spark Plasma Sintering of TiAl 48-2-2 powder, Intermetallics. 86 (2017) 147–155. https://doi.org/10.1016/j.intermet.2017.03.006.

[33] U. Hofmann, W. Blum, Kinetics of high temperature deformation of lamellar Ti48Al-2Nb-2Cr, Intermetallics. 7 (1999) 363–369. https://doi.org/https://doi.org/10.1016/S0966-9795(98)00124-1.

[34] C. Manière, E.A. Olevsky, Porosity dependence of powder compaction constitutive

parameters: Determination based on spark plasma sintering tests, Scr. Mater. 141 (2017) 62–66. https://doi.org/10.1016/j.scriptamat.2017.07.026.

[35] T. Zhou, L. Peng, Y. Liu, Y. Zhan, F. Liu, A. Zhang, An insight into the sequential order in 2D correlation spectroscopy using polymer transitions: Boltzmann Sigmoid, Gaussian Cumulative, Lorentz Cumulative, and Asymmetric Sigmoid. Findings in experiments and simulations, Vib. Spectrosc. 70 (2014) 137–161. https://doi.org/10.1016/j.vibspec.2013.12.001.